Preprint typeset using LaTeX style emulateapj v. 04/21/05

THE SDSS COADD: 250 DEG^2 OF DEEP SDSS IMAGING ON STRIPE 82

James Annis[1], Marcelle Soares-Santos[1], Michael A. Strauss[2], Andrew C. Becker[3], Scott Dodelson[1,8], Xiaohui Fan[4], James E. Gunn[2], Jiangang Hao [1], Željko Ivezić[3], Sebastian Jester[5], Linhua Jiang[4], David E. Johnston[1], Jeffrey M. Kubo[1], Hubert Lampeitl[6], Huan Lin[1], Robert H. Lupton[2], Gajus Miknaitis[7], Hee-Jong Seo[9], Melanie Simet[8], Brian Yanny[1]

ABSTRACT

We present details of the construction and characterization of the coaddition of the Sloan Digital Sky Survey Stripe 82 *ugriz* imaging data. This survey consists of 275 deg^2 of repeated scanning by the SDSS camera of 2.5° of δ over $-50° \leq \alpha \leq 60°$ centered on the Celestial Equator. Each piece of sky has ~ 20 runs contributing and thus reaches ~ 2 magnitudes fainter than the SDSS single pass data, i.e. to $r \sim 23.5$ for galaxies. We discuss the image processing of the coaddition, the modeling of the PSF, the calibration, and the production of standard SDSS catalogs. The data have r-band median seeing of $1.1''$, and are calibrated to $\leq 1\%$. Star color-color, number counts, and psf size vs modelled size plots show the modelling of the PSF is good enough for precision 5-band photometry. Structure in the psf-model vs magnitude plot show minor psf mis-modelling that leads to a region where stars are being mis-classified as galaxies, and this is verified using VVDS spectroscopy. As this is a wide area deep survey there are a variety of uses for the data, including galactic structure, photometric redshift computation, cluster finding and cross wavelength measurements, weak lensing cluster mass calibrations, and cosmic shear measurements.

Subject headings: atlases — catalogs — surveys

1. INTRODUCTION

The Sloan Digital Sky Survey (SDSS; York et al. 2000) saw first light in 1998 with the goal of obtaining CCD imaging in five broad bands *ugriz* over 10,000 deg^2 of high-latitude sky in the North Galactic Cap, plus spectroscopy of one million galaxies and one hundred thousand quasars over this same region. In addition, the SDSS imaged a 275 deg^2 region on the Celestial Equator in the Southern Galactic Cap. This region is called "Stripe 82" and was imaged multiple times during the Fall months when the North Galactic Cap was not observable. The SDSS single pass data reach $r \sim 22.4$ and has median seeing of $1.4''$ in r, but by aligning and averaging ("coadding") the Stripe 82 images we reached ~ 2 magnitudes deeper and median seeing of $\sim 1.1''$. The intent was to use this deep survey to understand the single pass data at its limits and to do science at fainter magnitudes or correspondingly higher redshifts. Such analyses benefit from our image processing approach, as opposed to catalog-level methods, because objects below the detection limit of individual single pass images can be detected and measured. A brief description of the Stripe 82 data and coadd was presented in the SDSS Seventh Data Release (DR7) paper (Abazajian et al. (2009); see also, Jiang et al. (2008)). Here we give a full report, detailing the features in he coaddition process.

The SDSS uses a dedicated wide-field 2.5m telescope (Gunn et al. 2006) located at the Apache Point Observatory (APO) near Sacramento Peak in Southern New Mexico. The telescope imaging instrument (Gunn et al. 1998) is a wide-field camera with 24 2048 × 2048 $0.396''$ pixel scale CCDs. SDSS images the sky in drift scan mode with the five filters in the order *riuzg* (Fukugita et al. 1996). Imaging is performed with the telescope tracking great circles at the sidereal rate; the effective exposure time per filter is 54.1 seconds, and 18.75 deg^2 are imaged per hour in each filter. The images are mostly taken under good seeing conditions on moonless photometric nights (Hogg et al. 2001). For stellar sources the 50% completeness limits of the images are $u, g, r, i, z = 22.5, 23.2, 22.6, 21.9, 20.8$, respectively (Abazajian et al. 2003), although these values depend on seeing and sky brightness. The image processing pipeline determines the astrometric calibration (Pier et al. 2003), then detects objects and measures their brightnesses, positions and shapes (Lupton et al. 2001; Stoughton et al. 2002). The astrometry is good to 45 milliarcseconds (mas) rms per coordinate at the bright end (Abazajian et al. 2009). The photometry is calibrated to an AB system (Oke & Gunn 1983), and the zero-points of the system are known to 1–2% (Abazajian et al. 2003, 2004). The photometric calibration is done in two ways, by tying to photometric standard stars (Smith et al. 2002) measured by a separate 0.5m telescope on site (the PT telescope; Tucker et al. 2006; Ivezić et al. 2004) and by using the overlap between adjacent imaging runs to tie the photometry of all the imaging observations together, in a process called "ubercalibration" (Padmanabhan et al. 2008). Ubercalibration zero-points on each stripe have rms error of $\sim 2\%$ in u and $\sim 1\%$ in *griz*.

[1] Center for Particle Astrophysics, Fermi National Accelerator Laboratory, P.O. Box 500, Batavia, IL 60510, USA
[2] Department of Astrophysical Sciences, Princeton University, Princeton, NJ 08544, USA
[3] Department of Astronomy, University of Washington, Box 351580, Seattle, WA 98195, USA
[4] Steward Observatory, 933 North Cherry Avenue, Tucson, AZ 85721, USA
[5] Max Planck Institut für Astronomie, Königstuhl 17, 69117 Heidelberg, Germany
[6] Institute of Cosmology and Gravitation, University of Portsmouth, Portsmouth, PO1 3FX, UK
[7] Dill Pickle Food Co-op, 3039 W. Fullerton, Chicago, Il USA
[8] Kavli Institute for Cosmological Physics, Chicago, IL USA
[9] Berkeley Center for Cosmological Physics, LBL and Department of Physics, Universityof California, Berkeley, CA, USA94720.

SDSS data is obtained as runs, where a run is a single continuous drift scan obtained on a single night. A survey stripe is one camera width wide, about 2.5°. Two interleaving runs called strips are necessary to complete a stripe as the camera focal plane is sparsely populated. These strips are denoted either N or S, depending if the telescope boresight is pointed half a CCD width north or south of the stripe equator. A run contains 6 columns of data through the five *ugriz* filters, and a single filter data set is called a scanline. Each scanline is a 13′ wide continuous stream of data that we arbitrarily chop into overlapping 10′ long frames. A frame is a single image in a single bandpass, and has a geometry of 1489 rows and 2048 columns, at a pixel scale of 0.396"/pixel. A field is the set of *ugriz* frames of the same piece of sky, disregarding the fact that they were obtained over 8 minutes of time. For Stripe 82 in particular, there is a unique mapping of RA and Dec into survey constructs. The row number of a field corresponds to RA, as does the field number. The column number of a field corresponds to Dec, as does the camera column number. The fields overlap along the RA direction by 124 rows per field due to a repackaging of the same pixel data during data acquisition. They overlap along the Dec direction by a small amount on either edge of the field due to re-observation of sky by slightly overlapping scanlines. The coadd runs are artificial, so we adopted run number 100006 as the south strip and 200006 as the north strip arbitrarily. These were later renamed as 106 and 206 for convenience. These runs interleave, but for constant column number, run 206 is at a higher Dec than run 106. Each run is 800 fields long and goes in increasing field number from the West to East, from low to high RA. For more information on the SDSS nomenclature and technical terms, see Stoughton et al. (2002).

Stripe 82 is the SDSS stripe along the Celestial Equator in the Southern Galactic Cap. It is 2.5° wide and covers $-50° \leq RA \leq +60°$, so its total area is 275 deg^2. Stripe 82 can be observed from APO at low airmass from September through November, is accessible from almost all ground-based telescopes for subsequent spectroscopic and photometric observations and, except near its RA ends, has low Galactic extinction (Schlegel et al. 1998). Stripe 82 was imaged by the SDSS multiple times in the Fall months and through 2004, these data were taken only under optimal seeing, sky brightness, and photometric conditions (i.e., the conditions required for imaging in the main Legacy Survey; York et al. (2000)). There were 84 such runs. In 2005-2007, 219 additional imaging runs were taken on Stripe 82 as part of the SDSS supernova survey (Frieman et al. 2008), designed to discover Type Ia supernovae at $0.1 < z < 0.4$. The supernova survey was carried out on most usable nights, with the exception of the five brightest nights around each full moon. Therefore, these data were often taken under less optimal conditions: poor seeing, bright moonlight, and/or non-photometric skies.

Both reduced images and catalogs from all 303 runs covering Stripe 82 were made available as part of the SDSS DR7 (Abazajian et al. 2009), in a database called `Stripe 82`. The data can be accessed both the Data Archive Server (DAS) and the Catalog Archive Server (CAS). We carried out a coaddition of the repeat imaging scans, photometric or not, on Stripe 82 taken through Fall 2005. Data taken after that date were excluded as for the most part they had not been taken when we were processing the coadd. The coaddition includes a total of 123 runs, covering any given piece of the 275 deg^2 area between 20 and 40 times. The S and N strip runs are designated 100006 and 200006, respectively, in the DAS, and 106 and 206 in the CAS database.

We designed the coaddition program so that the output image format allowed us to run the SDSS standard measurement code, `PHOTO` (Lupton et al. 2001; Stoughton et al. 2002; Lupton et al. 2012), on the coadd images. This was important because: a) `PHOTO` has algorithms which had been extensively tested by the SDSS collaboration over the years; and b) the resulting data products are conveniently structured for joint analyses and comparisons with the single pass data. Our method considers the repeat scans of Stripe 82 to be noisy, distorted realizations of the true sky. The aim is to make our best estimate of the true sky as it would have been seen by a perfect SDSS camera on a larger telescope. Starting with the list of runs on Stripe 82 taken from the start of the survey to the Fall 2005 season, those fields of reasonable seeing (FWHM), transparency (T), and sky noise (σ_s) were selected for use in the coadd. The individual runs were remapped onto a uniform astrometric coordinate system. Interpolated pixels (due, e.g., to cosmic rays or bad columns) in each individual run were masked and the sky was subtracted from each frame. The images are coadded with weights that depend on FWHM, T and σ_s, providing optimal signal ratio to noise for point sources. `PHOTO` relies on an accurate point spread function (PSF) model for both stellar and galactic photometry (Lupton et al. 2001). Rather than remeasuring the PSF on the coadd images we computed the PSF by constructing the suitably weighted sum of the PSFs made by `PHOTO` for each run. The coadded images were run through `PHOTO` yielding the catalog made available in the CAS `Stripe82` database.

When using the coadd data for science it is important, just as with the main survey, to use the various processing flags associated with each detected object to reject spurious objects and to select objects with reliable photometry (as recommended, for example, by Richards et al. (2002)). Since the coadd data was run through the SDSS pipelines, the standard flag set is available for all objects. However, some objects at magnitudes < 15.5 that are saturated do not have the saturated flag set, so we recommend a magnitude cut to avoid them.

In this paper we first consider the observations (§2), then describe the coadd image (§3) and catalog creation (§4). In section §5 we present the results of our quality assurance tests and explore the features of this data set, highlighting the improvements in depth and seeing due to the coaddition process. We discuss the applications and science outcomes in §6 and conclude in §7.

2. OBSERVATIONS

Figure 1 shows the number of observations as a function of RA for runs 106 (S strip) and 206 (N strip) separately. The total number of images reaches ~ 100 for the S strip (blue, top curve) and ~ 80 for the N strip (black, top curve). About 30% of those runs are calibrated (red and black, bottom curves) in the sense that the infrared sky camera indicated a minimum of clouds

and a extinction solution was obtained for the 20" PT telescope data taken at the same night of the run. The final number of images used in the coadd, shown as thick green (N strip) and red (S strip) lines, varies from 15 to 34. The selection criteria to achieve this final sample is described in §2.1. Based on the number of observations used, we expect the coadd to be ~ 2 mag deeper than the single pass data and to show a difference of ~ 0.4 mag in depth between the shallowest and the deepest regions, assuming that the signal-to-noise ratio increases as $\sqrt{N}$.

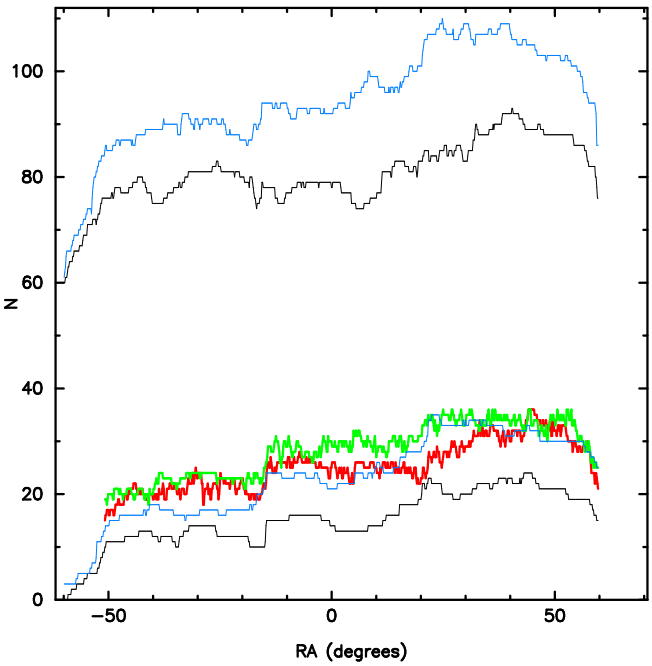

FIG. 1.— RA distribution of Stripe 82 observations for both runs 106 and 206, corresponding to S and N strips respectively. The total number of images reaches ~ 100 for the S strip (blue, top curve) and ~ 80 for the N strip (black, top curve). Nearly 30% of those are calibrated (red and black, bottom curves). The number of images selected for the coadd in both N (thick green) and S (thick red) strips varies from 15 to 34. We therefore expect to see a difference of ~ 0.4 mag in depth between the shallowest and the deepest regions of the coadd, assuming that the signal-to-noise ratio increases as $\sqrt{N}$. See text for details on the selection criteria.

2.1. *Field Selection Criteria*

The data selection criteria are listed in Table 1. We chose all runs on Stripe 82 with $125 \leq$ run ≤ 5924, i.e., all data obtained in or before December 1 2005, demanding that the runs were either on the N or S strip and rejecting ~ 10 runs that were not offset (strip labeled "O"), plus one run that is a crossing scan at $\sim 45°$ inclination. We then select the fields in r band, requiring seeing better than $2''$, sky brightness less than 19.5 mag/arcsec^2 and less than 0.2 mag of extinction. The sky brightness cut corresponds to 2.5 times the median sky of 150 DN, allowing at most 0.5 mag increase in sky noise. The majority of the data is uncalibrated so we also require that the field has enough stars for our relative calibration method to work. We cut on the r-band parameters, but rejected all the corresponding data in $ugiz$. This choice maximizes homogeneity across filters, though not optimization for a given filter.

The fraction of fields passing the seeing and sky noise cuts are 91% and 84%, respectively, and 77.5% pass both cuts jointly. However, 100% of the fields in the standard SDSS runs and 95% supernova fields pass the transparency cut and the demand to have enough stars to calculate the photometric scaling. This indicates that the SDSS had a high threshold for classifying a night as photometric. Overall, 1,124,075 frames were included in various fields of the coadd. The thick red and green lines in Fig. 1 shows the RA distribution of these selected frames.

Table 2 summarizes the 123 runs included in the coadd from both main survey and supernova runs. 69 of these were calibrated (phot=1), in the sense that the infrared sky camera indicated a minimum of clouds and a extinction solution was obtained for the PT telescope data. The remaining 54 runs were uncalibrated (phot=0). These were on average twice as long as the calibrated ones, as they were taken by the supernova survey which was unconcerned with photometricity or sky brightness.

Not all of the images in the available overlapping runs were used in a given coadded frame. In order to prevent sharp discontinuities in the PSF in the output image at input run edges, we imposed the constraint that if a field overlaps the output image, other good fields from the same run must cover the output image RA completely.

2.2. *Photometric Calibration*

The standard SDSS processing calibrates the single pass data using data obtained by the 20" PT telescope. These include a set of star fields in the Stripe 82 area and extinction values measured on the night the SDSS telescope data are obtained. The PT pipeline (Tucker et al. 2006) calibration results in runs calibrated to rms of 1% in gri, 2% in u and 3% in z, (Abazajian et al. 2003; Ivezić et al. 2004). The DR8 data (Aihara et al. 2011) includes the ubercalibration of Padmanabhan et al. (2008) which used Apache Wheel scans and runs obtained for Segue. The ubercalibration data were not available at the time this work was performed.

Much of the Stripe 82 data was non-photometric so we developed a method to calibrate them. In the process we also re-calibrated those runs taken under photometric conditions. The runs were calibrated following the prescription of Bramich et al. (2008), which builds a catalog-level coadd of bright stars to match stars in the frames and compute a zero-point shift. The resulting photometric calibration of a given run is good to 0.02 mag in up to 1 mag of atmospheric extinction (see also Ivezić et al. (2007) for a discussion of calibration through clouds).

The PT telescope observed the calibration patches in Stripe 82 many times while measuring the extinction for each standard run independently. Averaging stars calibrated using these independent calibrations will provide an increase in photometric accuracy. The increase is unlikely to be $\sqrt{N}$ as there are systematics floors from residual flat field variations and uncorrected atmospheric transmission variations.

We used 62 of the photometric runs for which normal SDSS PT calibrations were available to construct a standard star catalog. We start with a set of bright, isolated, unsaturated stars, with $14 < r < 18$, taken from a set of high quality photometric runs covering both strips of the whole stripe acquired over an interval of less than twelve

TABLE 1
Data Selection Criteria

Scope	Criterion	Description	Acceptance Rate
run	$125 \leq \mathrm{run} \leq 5924$	data taken on or before 12/1/2005 on Stripe 82	–
field	r $0.265\sqrt{\mathrm{neff_psf}} \leq 2.0$	seeing $< 2''$	91%
	r sky_frames ≤ 375 DN	sky brightness less than 19.5 mag/arcsec^2	84%
		2.5 × the median sky of 150 DN allowing at most 0.5 mag increase in sky noise	
	r transparency $> 1/1.2$	less than 0.2 mag of extinction	95%
	$\mathrm{N_{calibration}} \geq 1$	enough stars for relative calibration	95%

months (2659, 2662, 2738, 2583, 3325, 3388). We then match the individual detections of these stars in each of the 62 runs, using a matching radius of 1 arcsec. On average, there are 10 independent measurements of each star among the 62 runs, and we only include in the reference catalog those with 5 or more measurements. We then compute the mean of the independent calibrated flux measurements of each star and adopt that mean flux, defining it separately in each band. We use the fluxes measured in the SDSS "aperture 7", which has a radius of 7.43 arcsec; this aperture is typically adopted in the SDSS as a reference aperture appropriate for isolated bright star photometry.

Using this standard star catalog, we computed the relative zero-point offset of all fields in all runs used in the coadd, regardless of whether they were photometric or non-photometric runs initially. The relative zero-point offset was defined as the median fractional flux difference of the standard stars in each field in the run. These field-by-field offsets are the atmospheric transmission T, which we need for weighting in the coadd as well as to place the fields onto the same calibration. There is no requirement that T be a smooth function of RA as for example T will change with time on non-photometric nights.

The u band images have signal-to-noise ratio significantly poorer than the other bands and require special treatment. All u runs have a provisional calibration applied, but in case of non-photometric runs these calibrations are purely the average instrumental zero-point. We use this approximate calibration to eliminate lower signal-to-noise stars by rejecting those with $u > 18$. The remaining stars are used to match against the standard star catalog to find the relative zero-point.

The flux calibrations are relative magnitude offsets from a zero-point, -23.90. We interpret them as variations in T with respect to the mean transparency. We build a table of linear values of these relative flux scale factors T. We T in the coadd image creation process to place the images onto the system where the atmosphere has a uniform transparency, incorporating both zero-point and extinction from the all-sky-photometry model of the sky.

TABLE 2
Runs used in the coadd

run	MJD	date	$\mathrm{RA_{start}}$	$\mathrm{RA_{end}}$	strip	phot
125	51081	1998/09/25	-10.49	76.00	S	1
1033	51464	1999/10/13	-49.00	-9.40	N	1
1056	51467	1999/10/16	-35.32	-0.12	S	1
1752	51818	2000/10/01	21.45	79.13	N	1
1755	51819	2000/10/02	-55.68	47.42	S	1
1894	51875	2000/11/27	31.68	58.91	S	1
2385	52075	2001/06/15	-53.59	-37.64	N	1
2570	52170	2001/09/18	17.45	59.99	N	1
2578	52171	2001/09/19	29.06	61.44	N	1
2579	52171	2001/09/19	36.46	60.56	S	1
2583	52172	2001/09/20	-56.42	-16.95	S	1
2585	52172	2001/09/20	-32.85	-17.43	S	1
2589	52173	2001/09/21	15.79	62.58	N	1
2649	52196	2001/10/14	-17.58	10.29	N	1
2650	52196	2001/10/14	4.18	31.14	N	1
2659	52197	2001/10/15	-58.26	-34.58	N	1
2662	52197	2001/10/15	-41.69	39.74	N	1
2677	52207	2001/10/25	4.25	39.91	N	1
2700	52224	2001/11/11	20.73	63.92	N	1
2708	52225	2001/11/12	-15.63	25.61	N	1
2709	52225	2001/11/12	20.40	63.25	S	1
2728	52231	2001/11/18	-61.21	34.24	N	1
2738	52234	2001/11/21	12.86	62.18	N	1
2768	52253	2001/12/10	-17.40	35.82	N	1
2820	52261	2001/12/18	20.66	61.32	N	1
2855	52282	2002/01/08	19.76	30.66	N	1
2861	52283	2002/01/09	32.84	66.17	N	1
2873	52287	2002/01/13	14.21	62.59	N	1
2886	52288	2002/01/14	14.21	62.52	S	1
3325	52522	2002/09/05	-15.54	61.16	S	1
3355	52551	2002/10/04	19.37	61.00	S	1
3360	52552	2002/10/05	-53.45	25.70	S	1
3362	52552	2002/10/05	20.47	57.45	N	1
3384	52557	2002/10/10	-54.65	66.50	N	1
3388	52558	2002/10/11	-47.22	62.66	S	1
3427	52576	2002/10/29	-51.41	-24.96	S	1
3430	52576	2002/10/29	20.76	40.16	S	1
3434	52577	2002/10/30	-52.22	36.25	S	1
3437	52578	2002/10/31	-50.78	24.99	N	1
3438	52578	2002/10/31	30.63	62.61	S	1
3460	52585	2002/11/07	19.41	61.44	S	1
3461	52585	2002/11/07	42.77	61.24	N	1
3465	52586	2002/11/08	-34.17	21.68	S	1
4128	52908	2003/09/26	-7.82	61.45	N	1
4136	52909	2003/09/27	27.90	60.79	S	1
4145	52910	2003/09/28	-16.01	61.85	S	1
4153	52911	2003/09/29	-16.34	11.87	N	1
4157	52912	2003/09/30	19.23	61.20	N	1
4184	52929	2003/10/17	-52.92	-10.08	N	1
4187	52930	2003/10/18	-51.72	-34.03	S	1
4188	52930	2003/10/18	-15.85	8.25	N	1
4192	52931	2003/10/19	-52.66	23.32	S	1
4198	52934	2003/10/22	-53.56	61.16	N	1
4203	52935	2003/10/23	-60.00	61.51	S	1
4207	52936	2003/10/24	-55.00	61.38	N	1
4247	52959	2003/11/16	-15.67	28.74	S	1
4253	52962	2003/11/19	-15.59	13.24	N	1

TABLE 2 — *Continued*

run	MJD	date	RA_{start}	RA_{end}	strip	phot
4263	52963	2003/11/20	-16.70	53.98	S	1
4288	52971	2003/11/28	19.27	46.65	S	1
4797	53243	2004/08/26	-53.53	-24.28	N	1
4868	53286	2004/10/08	-30.53	62.90	N	1
4874	53288	2004/10/10	-62.40	88.08	N	1
4895	53294	2004/10/16	-4.80	70.77	N	1
4905	53298	2004/10/20	0.38	72.29	N	1
4917	53302	2004/10/24	-65.59	52.81	N	0
4930	53313	2004/11/04	-58.01	1.81	S	1
4933	53314	2004/11/05	-53.70	63.36	N	1
4948	53319	2004/11/10	7.31	62.39	N	1
5042	53351	2004/12/12	18.42	61.43	S	1
5052	53352	2004/12/13	-15.67	25.72	S	1
5566	53616	2005/09/03	-33.61	60.28	N	0
5582	53622	2005/09/09	-55.62	58.95	S	0
5590	53623	2005/09/10	-60.69	12.78	N	0
5597	53625	2005/09/12	-64.68	-17.02	S	0
5603	53626	2005/09/13	-66.47	63.02	N	0
5607	53627	2005/09/14	-63.90	62.25	S	0
5610	53628	2005/09/15	-66.73	65.38	N	0
5619	53634	2005/09/21	-64.44	63.20	S	0
5622	53635	2005/09/22	-64.48	63.38	N	0
5628	53636	2005/09/23	-64.61	21.61	S	0
5633	53637	2005/09/24	-61.59	59.71	N	0
5637	53638	2005/09/25	-21.61	63.42	S	0
5642	53639	2005/09/26	-10.71	62.83	N	0
5646	53640	2005/09/27	-65.64	70.65	S	0
5658	53641	2005/09/28	15.19	56.03	N	0
5666	53643	2005/09/30	40.36	63.58	S	0
5675	53645	2005/10/02	-60.60	-40.41	S	0
5681	53646	2005/10/03	22.34	54.21	S	0
5709	53654	2005/10/11	-67.46	24.71	N	0
5713	53655	2005/10/12	-68.40	42.80	S	0
5731	53657	2005/10/14	20.28	62.34	N	0
5732	53657	2005/10/14	46.22	62.33	S	0
5754	53664	2005/10/21	-57.68	59.33	S	0
5759	53665	2005/10/22	-59.55	59.24	N	0
5763	53666	2005/10/23	-59.22	5.29	S	0
5765	53666	2005/10/23	1.41	56.19	N	0
5770	53668	2005/10/25	-56.57	59.20	N	0
5771	53668	2005/10/25	32.20	62.16	S	0
5776	53669	2005/10/26	-59.98	59.26	S	0
5777	53669	2005/10/26	23.52	59.29	N	0
5781	53670	2005/10/27	-56.20	59.17	N	0
5782	53670	2005/10/27	31.77	62.19	S	0
5786	53671	2005/10/28	-36.66	63.30	S	0
5792	53673	2005/10/30	-62.44	59.30	N	0
5797	53674	2005/10/31	-59.00	59.39	S	0
5800	53675	2005/11/01	-59.49	59.98	N	0
5807	53676	2005/11/02	-48.55	59.20	S	0
5813	53677	2005/11/03	-65.13	45.97	N	0
5820	53679	2005/11/05	-45.43	62.22	S	0
5823	53680	2005/11/06	-60.09	62.32	N	0
5836	53681	2005/11/07	-60.56	62.35	S	0
5842	53683	2005/11/09	-59.31	62.22	N	0
5847	53684	2005/11/10	-63.50	63.90	S	0
5866	53686	2005/11/12	17.32	63.41	N	0
5878	53693	2005/11/19	-62.67	64.29	N	0
5882	53694	2005/11/20	-63.69	63.13	S	0
5889	53696	2005/11/22	35.34	63.13	S	0
5895	53697	2005/11/23	-63.25	62.62	S	0
5898	53698	2005/11/24	-65.81	62.31	N	0
5902	53699	2005/11/25	-62.81	62.75	N	0
5905	53700	2005/11/26	-68.06	62.74	S	0
5918	53704	2005/11/30	-62.39	62.28	N	0
5924	53705	2005/12/01	-63.20	62.51	S	0

3. COADD IMAGE CREATION

We aim at coadding the Stripe 82 data and running it through `PHOTO`. To make the coadd we need the data images and weight maps. We build a weight map by multiplying an inverse variance map and a geometry mask. `PHOTO` requires a map of the saturated pixels. In this section detail the process of creation of each of these image components and describe how we use them in the coaddition.

3.1. *Sky Subtraction*

The sky brightness varies both spatially and temporally, night to night and due to clouds. We removed the sky before mapping. As the data we used for the coadd came from DR7 and earlier, the improved sky subtraction of the current DR8 `PHOTO` was not implemented (Aihara et al. (2011); see also Blanton et al. (2011) for continued work on this subtle problem). The DR7 `PHOTO` algorithm, which was current at the time, produced a sky image by calculating the median of the 256×256 pixel boxes in the data image on a grid of 128 pixels in each dimension. The sky was then determined using bilinear interpolation. This algorithm over-subtracts the extended parts of galaxies on the scale of the 128×128 pixel grid used in the sky calculation, leaving artifacts due to astrophysical objects in the data. `PHOTO` sky subtraction engine was therefore deemed not suitable for our purposes and we developed our own method.

Subtracting a global sky for each frame would work poorly as the sky changed with time and thus with row number in the SDSS data. Instead we adopted a sky value that was allowed to vary linearly with row number and thus time. For a given frame and the two frames on either side of it in the run (and after removing the SDSS soft bias of 1000 DN), the median of the 2048 pixels along each row was calculated, resulting in a 3×1489 pixel sky vector. This vector is a time series estimate. In order to deal with bright stars, the rms of the vector was calculated using a 3σ 5 iteration sigma clipping, and the rms was used to reject pixels more than 2σ from the mean. A linear least squares fit to the remaining vector was used to model the sky, which was subtracted from the image row by row.

3.2. *Astrometry*

The coadd relies on the existing astrometry produced using the `astrom` pipeline (Pier et al. 2003). All of the images used in the coadd had astrometric calibrations. Pier et al. (2003) were able to achieve positions accurate to ~ 45 mas rms per coordinate by calibrating to the US Naval Observatory CCD Astrograph Catalogue (UCAC; Zacharias et al. (2000)). The accuracy is limited primarily by the accuracy of the UCAC positions (~ 70 mas rms at the UCAC survey limit of $R \approx 16$) and the density of UCAC sources. This accuracy can be represented in the affine transformations that are standard in the WCS convention. Pier et al. (2003) also noted that there are systematic optical distortions due to the camera present in the data. We will use the `astrom` measurements to remove these distortions.

The process of forward mapping requires a transformation from RA,Dec (α,δ) to pixel location in the input image. The SDSS runs were taken along great circles. Thus `astrom` worked in a coordinate system in which each run's great circle is the equator of the coordinate system. In this great circle coordinate system, the latitude of an observed star never exceeds about 1.3°; thus the small angle approximation may be used and lines of constant longitude are, to an excellent approximation, perpendicular to lines of constant latitude. Longitude

and latitude in great circle coordinates are referred to as μ and ν, respectively. ν is equal to 0 along the great circle, μ increases in the scan direction, and the origin of μ is chosen so that $\mu = \alpha_{2000}$ at the ascending node (where the great circle crosses the J2000 celestial equator). The conversion from great circle coordinates to J2000 celestial coordinates is then

$$\tan(\alpha - \mu_0) = \frac{\sin(\mu - \mu_0)\cos\nu\cos i - \sin\nu\sin i}{\cos(\mu - \mu_0)\cos\nu} \quad (1)$$

$$\sin(\delta) = \sin(\mu - \mu_0)\cos\nu\sin i + \sin\nu\cos i \quad (2)$$

where i and μ_0 are the inclination and J2000 right ascension of the great circle ascending node, respectively. $\mu_0 = 95°$ for all survey stripes, and for Stripe 82 $i \approx 0$.

Given the great circle coordinates (μ, ν) we can transform to distortion corrected frame coordinates (x',y') using the affine transformation

$$\mu_{CMP} = a + bx' + cy' \quad (3)$$

$$\nu_{CMP} = d + ex' + fy' \quad (4)$$

The transformation from (x', y') to (x, y) accounts for optical distortions which, in drift-scan mode, are a function of column only:

$$x' = x + g_0 + g_1 y + g_2 y^2 + g_3 y^3 \quad (5)$$

$$y' = y + h_0 + h_1 y + h_2 y^2 + h_3 y^3 \quad (6)$$

Equations (1-6) provide the pixel coordinates on the input image that corresponds to a given (RA,Dec) position.

Bramich et al. (2008) performed a recalibration of the Stripe 82 astrometry using a run from the mid-time of the Stripe 82 observations as a reference. This removed an erroneous but measurable galaxy mean proper motion of ~ 10 mas/yr in both RA and Dec due the proper motion of reference stars (see Bramich et al. (2008), Fig. 4). The optics distortions removed in this section have a maximum peak to peak shift of 80 mas (see Pier et al. (2003), Fig. 2) and are larger than the astrometry shifts induced by stellar motion over the 5 year range of the data used in the coadd. Therefore, although ideally we should have removed the reference star proper motion drift, in practice these have little effect.

3.3. *Astrometric Mapping of Data Images*

We geometrically map the input images onto the output image. We defined output frames aligned along the J2000 equator with rows aligned perpendicular to RA, in a standard SDSS image format, from $-50° \leq \alpha \leq 60°$ and $-1.25° \leq \delta \leq 1.25°$.

Since the output image is simply a locally flat tangent projection of the sky, the mapping must remove optical distortions and provide a surface brightness estimate at the aligned pixel location. To perform the mapping we used a version of Swarp (Bertin et al. 2002) modified to perform the astrometric conversions described in §3.2.

Each pixel in the mapped image is estimated from the input image pixels using a Lanczos interpolation kernel, which is a truncated sinc interpolation. Given bandwidth limited signal of infinite extent, sinc function interpolations reproduce exactly the data after resampling. Our data is not undersampled (it has $0.4''$ pixels and seeing of $\sim 1.3''$), but it is not of infinite bandwidth either and this motivates the use of a truncated kernel.

We used a two dimensional Lanczos-3 kernel retaining 3 maxima on each side of the center in each dimension. The one dimensional Lanczos-3 kernel is $L(x) = sinc(x)sinc(x/3)$, for $-3 < x < 3$. Then the 2 dimensional interpolation formula is

$$\hat{I}(r,c) = \sum_{i,j} I(i,j)L(r-i)L(c-j) \quad (7)$$

where r, c are the output image pixel coordinate and i, j are the input image pixel coordinate. The Lanczos-3 window is well-behaved in terms of reduction of aliasing, minimal ringing, and lack of smoothing, but a Lanczos-3 interpolation does use $(2x3+1)^2 = 49$ pixels to estimate the value of one output pixel. This is too large to use for bad pixels (e.g, saturated pixels), so we use nearest neighbor interpolation and reduce the weight of bad pixels during Lanczos-3 interpolation by using a mask (see section §3.8).

3.4. *Inverse Variance Map*

To keep track of the variance of data images, pixel by pixel inverse variance images are a natural choice, but they produce biases in the resulting mean. At low signal to noise the upward fluctuations in signal are given more weight than downward fluctuations as a result of the one-sided nature of the Poisson distribution. This bias is deterministic and one could correct for it, but, for example, for u-band data with its $120e^-$ of sky noise, pixels at 1σ above sky would be biased by 0.5% and this would be a fair fraction of our photometric error budget. Another problem is that per-pixel inverse variance weighting systematically changes the shape of the PSF as a function of the magnitude of the object. This would cause serious complications to our PSF-based photometry using `PHOTO`. For these reasons we chose a different method.

We computed the variance of the sky as measured on the frame from the width of the sky histogram. As we used a linear gradient sky subtraction, each image is assigned a variance image that is the variance of the subtracted linear sky gradient. This of course assumes Poisson statistics while the data are in ADU. In calculating this variance we did not include the effective gain, $g_{\rm eff}$, so gain variations are not accounted for. These variations are $< 30\%$ though.

3.5. *Geometry Mask*

The geometry mask, keeps track of which pixels in the input image actually contribute to the coadd. In this mask definition we account for image defects found by `PHOTO`, in particular, cosmic rays, saturated pixels and bad columns.

`PHOTO` produces a 16 bit mask image, the `fpM` file. For the geometry mask we are interested in the INTERP bit. The INTERP flag is set for any pixel for which `PHOTO` used interpolation to fill its value. This happens for cosmic rays, saturated pixels, and bad columns. These pixels are poor but not useless estimates of the true value of the pixel. We set the geometric weight of such pixels to a small value, 0.0000001. This ensures that if there is no input image which contributes a good estimate for a given output frame pixel, such as the center of a saturated star, the interpolated value is used.

The geometry of the SDSS images are also encoded into the geometry mask. In SDSS images, the first 124 rows of each frame are duplicates of the last 124 rows of the preceding frame. This replication of pixels was done so that objects could be well measured despite being on edge of a frame. To account for this, the first 124 rows of the mask are set to 0. In the SDSS images there are also scanline to scanline overlaps between North and South strips. This is actual exposure time, again designed to make objects on the edges measurable. For our purposes we kept the North and South strip data separate as the extra exposure was on too thin a strip to be useful.

3.6. *Satur Mask*

`PHOTO`'s bit mask also contains information about saturated pixels, encoded in the SATUR bit. The SATUR flag is set for any pixel that `PHOTO` determines to be saturated. We set these pixels to 1 in an image otherwise filled with zeros. This is the SATUR map, which we need for running `PHOTO` on the coadded images.

3.7. *Weight Map*

Although closely related, the weigh map and the inverse variance image are not the same. The weight map is the inverse variance image multiplied by the geometry mask. We set all masked non-zero pixels to the INTERP flag value (0.0000001). This allows us to keep track of the pixels altered by the masking.

We use the weigh map as input for the coaddition process, in which a weighted clipped mean of the data images, all mapped onto the same output image, will be performed. In addition, we coadd the inverse variance images and the satur maps as well, and although for those we use straight sums, the weigh map plays a role in the sense that only the pixels that pass the clipping for the data coadd are included (for details, see section §3.9.2).

3.8. *Astrometric Mapping of Map & Mask Images*

The inverse variance map, satur mask and weight map are all mapped onto the same output image as the data. For the inverse variance and weight images we apply the same Lanzcos-3 interpolation used for the data in order to replicate the noise correlation. The satur masks, propagating saturated pixels, were mapped using a nearest neighbor interpolation. This is more suitable than Lanzcos-3 because masked pixels an area of influence limited to their first neighbors.

In the process of performing the wide Lanzcos-3 interpolation of the data, the geometry mask is used to prevent masked pixels from contributing to the interpolation with more than minimal weight. In addition, once the images are mapped onto the output image, any non-overlap is set to zero weight using the geometry mask.

After this mapping procedure, each stack of images is ready for the coaddition process. No scaling has been done at this stage, so the stack for a given output image can be further filtered and/or weighted as needed.

3.9. *Coaddition*

With the four stacks of images (data, inverse variance, weight and satur) all aligned and cropped to match the output image, we have all the inputs needed to produce the coadded images and run `PHOTO` on them. We chose to use all the data in our image set. This allows us to maximize the depth of the coadd data.

Alternatively, one could devise a selection criteria to produce a coadd dataset tailored for a specific purpose. For example, one could select only images with the best seeing and limit them in number to form a uniform depth, aiming at weak lensing studies.

3.9.1. *Weights*

The data in our image set is of variable quality and we wish to optimize our coadd, so we designed a weighting scheme. The signal to noise ratio of the measurement of flux from a star is:

$$S/N \propto \frac{N_{\rm photons}}{\sqrt{A_{\rm psf}}\sigma_{\rm sky}} \tag{8}$$

where $N_{\rm photons}$ is the number of photons detected from the source, $A_{\rm psf}$ is the area in pixels the source subtends, and σ_{sky} is the sky noise per pixel. As N is proportional to transparency T and $A \propto \mathrm{FWHM}^2$, we use the following as weights:

$$w_i = \frac{T_i}{\mathrm{FWHM_i}^2 \sigma_i^2(p_i)} \tag{9}$$

This gives highest weight to good seeing data taken when the sky is clear and dark. We choose these weights because although the usual inverse variance weighting produces the minimum variance image, the signal to noise for a star depends on square of seeing. With this weight, the PSF of the coadd is $0.3''$ less than the median of the input images in *ugri* and $0.2''$ less in z.

We take the seeing for each field and filter from the `tsField` file, which is simply an average over the frame, and use it regardless of how much the frame contributes to a given output coadd frame. The transparency T, in turn, is already available as a product of the photometric calibration discussed in section §2.2. We have therefore cataloged for each image the transpareancy, the seeing, and via the inverse variance image, the sky variance. This allows us to proceed to the coaddition.

3.9.2. *Weighted Clipped Mean*

We coadd by building the stack of mapped images on a given output frame and performing a weighted clipped mean. The weight images described in §3.7 are multiplied by T/FWHM^2. Flux calibration of our data images by $1/T$ means that our weight images get another factor of T^2 due to error propagation.

Then for each output pixel we collect the corresponding mapped pixels, and reject outliers, using a iterative 5σ rejection, where for "σ" we use the 25-75% interquartile range The final average uses the weights of Eq. 9.

The data images are coadded as described above. The inverse variance image and the satur mask coadds were computed using straight sums (not averages), though using only those pixels corresponding to those that make it past the clipping process into the coadded data image.

3.10. *Output Images*

Figure 2 shows a side by side comparison between coadd single pass data in r-band. The single pass counterpart is one out of 28 images used in the coaddition

which means that it passed all the cuts discussed in the text. This example features run 206, camcol 3, field 505 in r-band. It illustrates the fact that a number of objects bellow the detection threshold of each image can be well detected and measured in the coadd. The seeing, however, is larger for the coadd image in this example, indicating that this particular single pass image has seeing better then the median seeing on the stack.

4. CATALOG CREATION

The coadd production yields 800 fields along six columns in each of two stripes and each field includes data in five bands. The resulting 48,000 images are processed through a modified version of the SDSS image processing pipeline PHOTO, to yield object catalogs.

4.1. *PSF Measurement*

Our principal challenge is to measure the PSF of the coadd. The PSF of SDSS images varied in time, corresponding to image rows, due to atmospheric fluctuations. It also varied in space, corresponding to columns, due to camera optics. In the standard single run reduction, PHOTO fits the spatial variation of the PSF by computing a PSF basis set using a Karhunen-Loéve (KL) expansion. The stars in the frame and the two flanking on either side (five in total) are used to determine the KL basis functions $B_R(u,v)$:

$$P_i(u,v) = \sum_{r=1}^{r=n} a_i^r B_R(u,v) \tag{10}$$

where P_i is the PSF of the ith star, u, v are the pixel coordinates relative to the basis function origin, and n sets the number of terms to use in the expansion (we use $n = 3$). The stars in the image and the flanking half an image on either side (two in total) are used to determine the KL coefficents a_i^r:

$$a_i^r \approx \sum_{l=m=0}^{l+m\leq N} b_{lm}^r x_i^l y_i^m \tag{11}$$

where x, y are the coordinates of the center of the ith star, N is the highest power of x or y included in the expansion (we use $N = 2$, a quadratic spatial variation of the PSF), and the b_{lm}^r are found by minimising

$$\sum_i (P_i(u,v) - \sum_{r=1}^{r=n} a_i^r B_r(u,v))^2 \tag{12}$$

In the coadd we took advantage of the fact that the KL basis set and coefficients had already been determined each input image as each of the input runs had already been separately processed through PHOTO. Using the KL basis set for each input run corresponding to the given output frame and the two flanking frames, we compute a weighted sum of the model PSFs (using the weights of equation 9) on a 2-dimensional grid with a spacing of $\sim 1.5'$. We then fit the KL basis $B_R(u,v)$'s to these over the coadd frame and the two flaking frames. The computation of the coefficents of the PSF expansion a_i^r are done on the coadd frame and the two flanking half-frames as in the single pass runs, with the exception that we set the maximum number of coefficients, n in Eq. 10, to $n = 4$ and highest power of x, y, N in Eq. 11, to $N = 3$.

4.2. *Effective Gain & Sky*

PHOTO had to be modified to read in a file containing the weights and effective gains of the images. The effective gain of a coadd image G should be such that it gives bright objects Poisson statistics for the variance associated with a source when scaling the averaged pixel counts back to electrons. Therefore,

$$\sigma^2(P) = P/G \tag{13}$$

where P is the weighted sum, over all exposures i, of the object counts p_i,

$$P = \sum w_i p_i = \sum w_i T_i o_i \tag{14}$$

and $p_i \equiv T_i o_i$ is the object's flux per exposure o_i times the flux scale factor T_i. The corresponding variance is:

$$\begin{aligned}\sigma^2(P) &= \sum w_i^2 \sigma^2(p_i) \\ &= \sum w_i^2 T_i^2 \sigma^2(o_i) \\ &= \sum w_i^2 T_i^2 o_i/g_i \\ &= \sum p_i w_i^2 T_i/g_i \end{aligned} \tag{15}$$

Assuming that p_i does not vary much from image to image, we obtain:

$$\sigma^2(P) \approx \langle p_i \rangle \sum w_i^2 T_i/g_i = P \sum w_i^2 T_i/g_i \tag{16}$$

Eqs. 13 and 16 we conclude that the effective gain is:

$$G = \left[\sum w_i^2 T_i/g_i\right]^{-1} \tag{17}$$

In the SDSS the gains g_i of all frames going into a single coadd frame are the same (it is always the same CCD), so they may be replaced by a single g outside the sum:

$$G = \frac{g}{\sum w_i^2 T_i} \tag{18}$$

To process the images with PHOTO we also need to compute the effective sky level S'. Assuming that dark and read noise are accounted for in the Poisson noise of the effective sky, we can easily obtain S' using the effective gain G calculated in Eq. 18 and the relation $S' = G\sigma^2(S')$, which is analogous to Eq. 13. We used the clipped variance of the coadd frame to compute $\sigma^2(S')$. Alternatively, one could take the sky variances and weights of the input frames and compute it using $\sigma^2(S') = \sum w_i^2 T_i^2 \sigma^2(s_i)$.

Using this method we obtained, for each field and for all 5 filters, the effective sky (S'), sky noise ($\sigma(S')$) and gain (G, Eq. 18). With these quantities in addition to the weights (w_i, Eq. 9) we processed all of the coadd fields through PHOTO.

4.3. *Applying the Calibration*

The SDSS code Target is used to apply the calibration to the raw outputs of PHOTO. Following Lupton et al. (1999), we convert from fluxes f to mags m using

$$m(f/f_0) = -\frac{2.5}{\ln 10}\left[\operatorname{asinh}\left(\frac{f/f_0}{2\,b}\right) + \ln(b)\right] \tag{19}$$

where b is an arbitrary dimensionless softening parameter below which the magnitude scale goes from linear to logarithmic and f_0 is a reference flux that sets the zero-point,

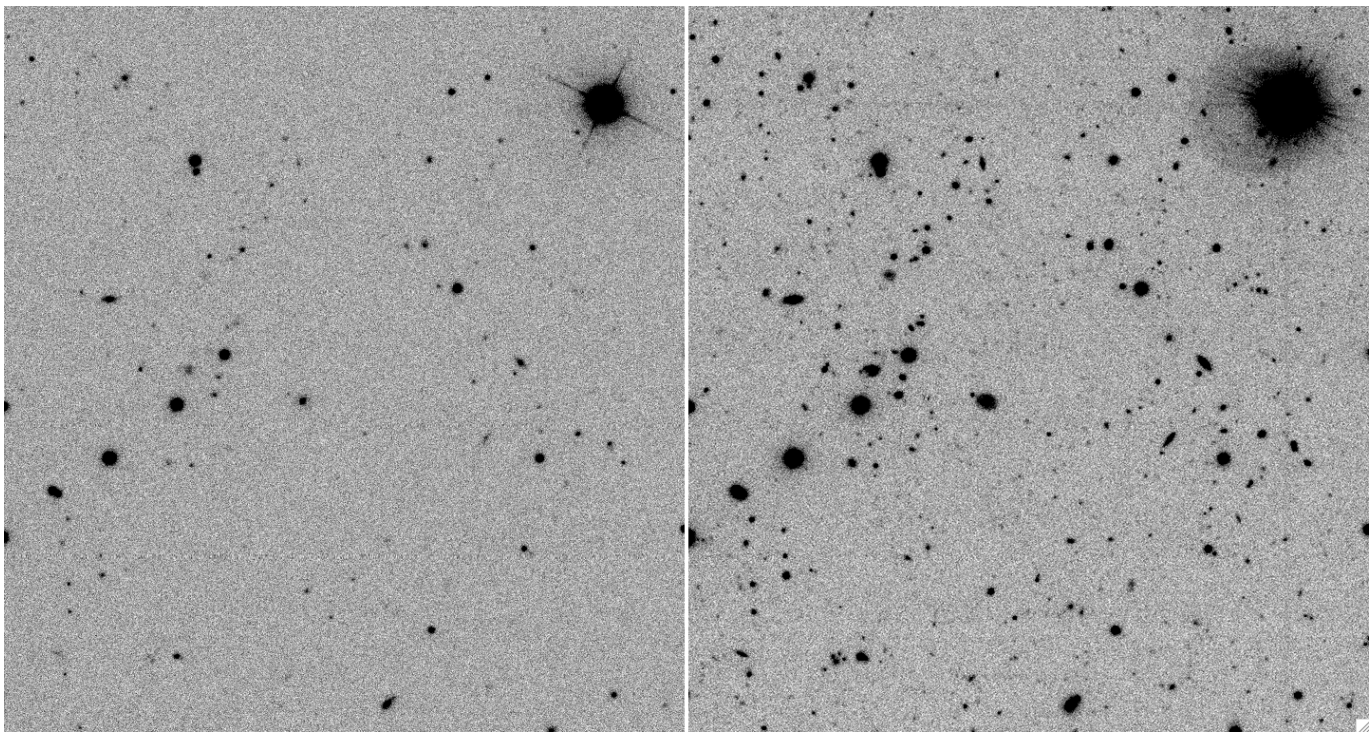

FIG. 2.— Comparison between single pass (left) and coadd (right) images in r-band for run 206, camcol 3, field 505, RA=15, Dec=0. Images are shown with the same scale, contrast and stretch. The single pass counterpart (run 5800, camcol 3, field 505) is one out of 28 images used in the coaddition of this particular image. This example illustrates the fact that a large number of objects bellow the detection threshold of each image can be well detected and measured in the coadd.

TABLE 3
ASINH MAGNITUDE SOFTENING PARAMETERS FOR THE COADD

filter	b	zp	$m(10b)$
u	1.0×10^{-11}	27.50	24.99
g	0.43×10^{-11}	28.42	25.91
r	0.81×10^{-11}	27.72	25.22
i	1.4×10^{-11}	27.13	24.62
z	3.7×10^{-11}	26.08	23.57

NOTE. — Values reported by Abazajian et al. (2009). Column zp is the zero-point magnitude, $zp \equiv m(0)$. The final column gives magnitude associated with an object for which $f/f_0 = 10b$.

$zp \equiv m(0)$, of the magnitude scale. The values of b that we used for the coaddition is given in Table 3, along with the asinh magnitudes associated with a zero flux object and the magnitudes corresponding to $f = 10 f_0 b$. Above this scale, the asinh magnitude and the traditional logarithmic magnitude differ by less than 1% in flux. These values can be compared to their equivalent numbers for the main survey, given in Table 21 of Stoughton et al. (2002). The coadd images were all placed onto a uniform flux scale such that 1 DN corresponds to a flux of 1 picomaggie, corresponding to a logrithmic (and not asinh) mag of 30.

4.4. *Star/Galaxy Separation*

The SDSS standard star/galaxy separation simply classifies as stars all objects in the region (Abazajian et al. 2004) $|r_{\rm psf} - r_{\rm model}| \leq 0.145$ where $r_{\rm model}$ is the model magnitude (the best fit galaxy deVaucouleurs or exponential profile convolved with the PSF) and $r_{\rm psf}$ is the PSF magnitude at the position of the object. This simple estimator performs well for single pass data: 95% correct at magnitude 21 in r.

In the case of the coadd data, star count plots showed dramatic increases in the numbers of stars at magnitudes where galactic models do not. This suggested that more numerous galaxies were being misclassified as stars there. Thus we instead used the more stringent criterion

$$|r_{\rm psf} - r_{\rm model}| \leq 0.03 \qquad (20)$$

to select stars. As `PHOTO` measures every parameter for every object regardless of its determination of object type this has no effect on the other measurements.

5. DATA PRODUCTS VERIFICATION

5.1. *Photometric Calibration*

We use the standard star catalog of Ivezić et al. (2007) to verify our photometric calibration. To build that catalog Ivezić et al. (2007) took the median of individual measurements of bright stars from 58 Stripe 82 runs and then applied several corrections to their catalog: 1) a color-term like correction for the bandpass of each camera column; 2) a purely RA flat field correction in r derived by comparing PT data with SDSS data; and 3) a purely Dec flat field correction to the colors relative to r band from stellar locus colors. We will take the resulting catalog (which is calibrated to 1% accuracy) as the truth and compare with our own measurements. As Ivezić et al. (2007) applied corrections that we did not, the comparison is not completely circular.

We sliced our star catalog into a series of 1 magnitude bins and matched to the Ivezić et al. (2007) catalog using a 1" matching radius and discarding objects with more

than one match inside that radius. No flags were applied to our star selection; in particular we did not demand an isolated, well measured set of stars to start with.

Table 4 summarizes the results of our comparison. We defined Δ_i as the median of the difference between our measurements and the quantities reported in the standard star catalog, for magnitudes ($i = m$) and colors ($i = c$). Δ_i is a measure of the zero-point offset. Statistical uncertainty in the zero-points, obtained as the rms of the differences, are of the order a few millimag/$\sqrt{N_{\rm obj}}$; as usual in photometry we can expect systematics to dominate this. The offsets from the standard zero-points are less than 5 millimags (1% photometry corresponds to 10 millimags) in all cases.

We also examined the spatial variations of the zero-point offset and its uncertainty. To this end, we first took 50 equally spaced bins of width 2.2° in RA, and computed the mean differences in magnitudes and colors for each bin. We repeated this procedure in Dec bins, choosing 30 bins of 5′ width. Figure 3 shows these mean zero-point offsets as a function of RA and Dec, indicating that spatial variations non-negligible, specially for u band. As a measure of the overall offsets we computed the median of those means, $\langle\Delta_i\rangle_j$, where j means either RA or Dec. These values are also included in Table 4 with the uncertainties estimated as the rms or the means.

Our comparison to the standard star catalog reveals, therefore, that along the RA axis in Stripe 82 the calibration varies 5 millimag in g, r, i, z, $g-r$, $r-i$, $i-z \leq 10$ millimag in u and $u-g$. Likewise, along the Dec axis the calibration varies by < 5 millimag in g, r, i, z, $g-r$, $r-i$, $i-z$and 30 millimag for u, 20 millimag for $u-g$and ≤ 10 millimag for the others. These can be seen in Fig. 3 (see also Table 4). The variation in Dec is significantly larger than that in RA, probably reflecting systematic errors in the PT flat field images and thus in the PT standard overlap fields the used for the calibration.

5.2. *PSF Modeling*

We verified how well we modeled the PSF in several ways, starting by computing the spatial variations in seeing, which can be written as

$$\mathrm{FWHM(arcsec)} = 2\sqrt{2\ln 2}\sqrt{\mathrm{mrrcc}/2}\cdot S \qquad (21)$$

where $S = 0.396''$ is the pixel scale and mrrcc is the sum of the second moments of the PSF. We used high S/N stars in each bandpass for this test. Our results, illustrated on the left panel of Fig. 4, show that the seeing is best in the redder filters, consistently with a Kolmogorov seeing law with the exception of r-band and i-band. We interpret this as an effect of selecting the input frames for the coadd in r-band (see Table 1) associated with an effect of the time scales of the Kolmogorov law. Recall that the data making up a field are taken at different times, ranging over 8 minutes from r-band to g-band. Our data support the assumption that the time scales of Kolmogorov seeing are such that the seeing is uncorrelated after ~ 1 minute, but since i and r are next to each other in the imager, they can be correlated. The median of the seeing of the single pass images are a few tenths of an arcsecond worse than the points on this plot; this reflects the weighting of the coadd (Eq. 9).

Figure 4 also show the seeing as a function of Dec, averaging over RA. The seeing is affected by the camera optics, which causes the upturn at one end of the camera, The N strip (run 206) has about $0.075''$ worse seeing in $ugiz$, and $0.15''$ worse seeing in r, then the S strip (run 106), presumably due to the statistics of the seeing in the input images. However, at Dec $\gtrsim +0.5°$, as the camera optics begin to dominate, the seeing difference becomes negligible.

Another interesting test of our PSF modeling is to check the reconstructed PSF at the position of stars. In Fig. 5 we show the mean ratio of `mrrcc` for stars and the reconstructed PSF at the locations of stars, as a function of Dec. The strong declination dependence seen in Fig. 4 is not apparent. This suggests that the modeling is fitting the spatial variation of the PSF well. We also found no correlation between the statistics of star galaxy separation and column number, again suggesting reasonable success in the PSF modeling.

However, given the importance of the PSF modeling for crucial aspects of the data, such as star/galaxy classification, accurate photometry and shape measurements, we examine it in more detail. A sensitive test of the PSF modeling is the r-band "PSF minus model" plot, $r_{\rm psf} - r_{\rm model}$ vs. $r_{\rm psf}$. This is shown in Fig. 6 for both stars (red) and galaxies (blue) (for details on the star/galaxy separation, see §4.4). Stars are expected to be found at a very narrow region around $r_{\rm psf} - r_{\rm model} = 0$. and this is clearly the case for the bright magnitudes in our plot. There is a noticeable trend towards negative values of $r_{\rm psf} - r_{\rm model} = 0$ at the faint end, around magnitude 23, and an upward spread at about magnitude 22. The upward spread cannot be due to galaxies behind stars causing the PSF to slightly broaden as this was excluded by checking the spatial statistics. These two features in the diagram suggest that we have magnitude dependent PSF fitting problems which may introduce systematics in analyses involving the coadd data.

While probing this, we found that during the processing described in section §3.9.2 the coadd incorrectly set the error propogation value to T instead of the correct value of T^2. This means that the weight actually used was:

$$w = \frac{1}{\mathrm{FWHM}^2\sigma^2} \qquad (22)$$

This has little effect on the coadded image as we only selected those images with $1/T \leq 1.2$. The PSF photometry, however, depends so sensitively on the modeled PSF that this may be the root of the problem. The PSFs were constructed using the correct weights (section §4.1), but these differed from those of the images. In an experiment we ran `Photo` with input weights that were pure inverse variance instead of SN weight that the images were built with. The resulting psf-model vs psf plots showed stars with deviations away from zero at 0.05 mags/mag level. The effects we are seeing in Fig. 6 are at the ~ 0.01mags/mag level, consistent with the lower affect the tranmission has on the weights. We conclude that the low level psf problems that the structure in Fig. 6 indicates is due to this mismatch of weights between the coadd images and the coadd photometry measurements.

5.3. *Galaxy Catalog Purity*

These misclassified stars are an issue as they lie in the magnitude-color space of LRGs. The contamination

TABLE 4
RELATIVE ZERO-POINTS FOR SELECTED COADD CATALOG SAMPLES

filter	$N_{\rm obj}$	mag	Δ_m	color	Δ_c	$\langle\Delta_m\rangle_{\rm RA}$	$\langle\Delta_c\rangle_{\rm RA}$	$\langle\Delta_m\rangle_{\rm Dec}$	$\langle\Delta_c\rangle_{\rm Dec}$
u	1311	20-21	1.2 ± 1.6	u-g	-4.3 ± 3.6	-21.0 ± 8.2	-12.1 ± 8.1	-21.3 ± 28.8	-12.4 ± 15.3
g	1399	19-20	2.2 ± 1.6	g-r	-1.7 ± 1.4	6.5 ± 4.6	-1.2 ± 3.5	5.8 ± 10.2	-1.1 ± 6.3
r	3703	19-20	3.7 ± 1.5	r-i	-2.9 ± 2.2	3.2 ± 2.5	4.0 ± 2.1	3.2 ± 6.3	4.0 ± 4.1
i	7436	19-20	0.9 ± 2.0	i-z	-1.5 ± 2.3	0.1 ± 2.0	6.3 ± 3.1	1.0 ± 6.2	5.7 ± 6.8
z	3963	18-19	4.3 ± 2.4	···	···	-5.7 ± 3.3	···	-5.3 ± 11.7	···

NOTE. — Rows correspond to samples created independently for each filter. Magnitude ranges are indicated by the mag column. $N_{\rm obj}$ is the number of stars in each sample. Δ_i is the median zero-point difference, in millimags, for either magnitudes ($i = m$) or colors ($i = c$) and $\langle\Delta_i\rangle_j$ is the median of the mean difference in spatial bins, RA or Dec.

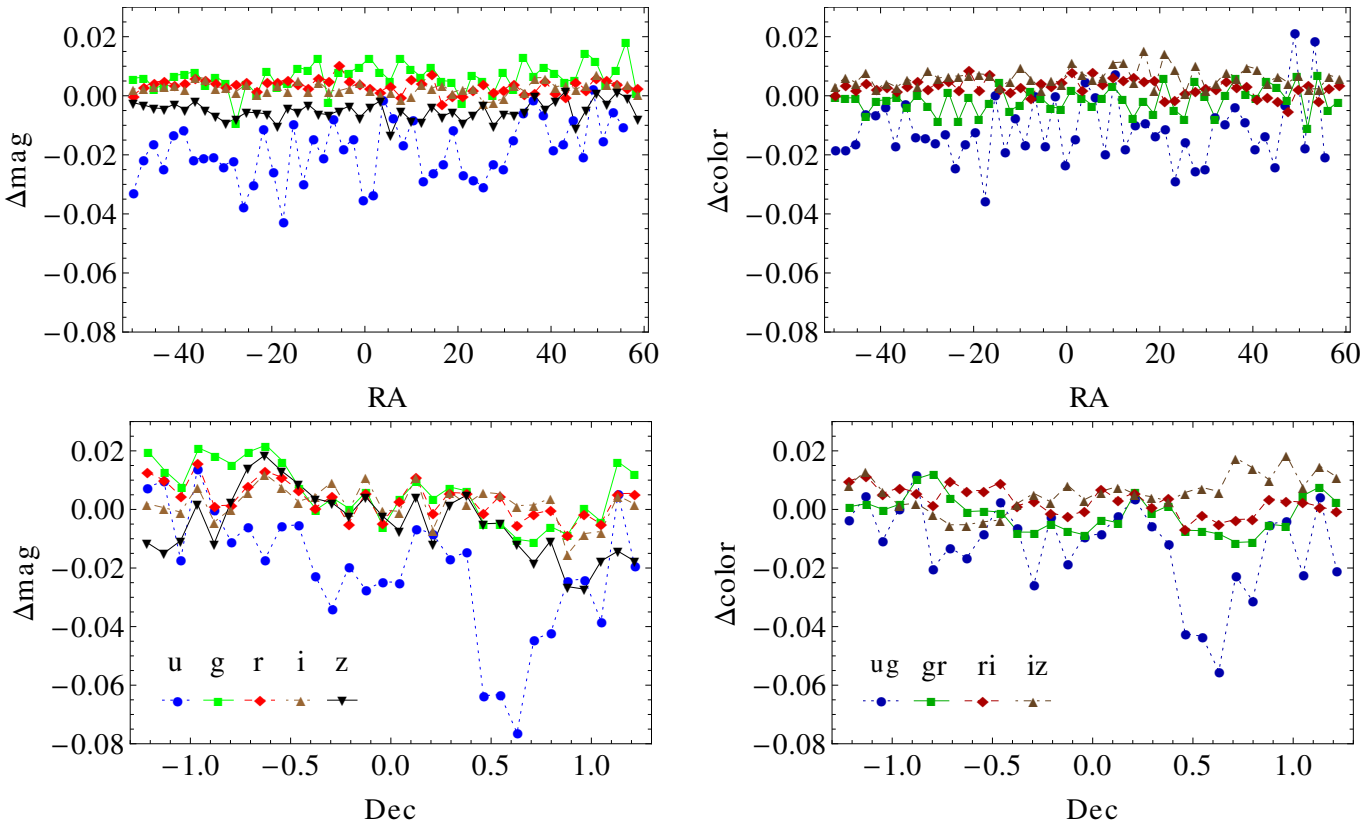

FIG. 3.— Zero-point offsets measured in bins of RA and Dec, showing spatial variations in the photometric calibration of the coadd data.

level of the galaxy catalog by missclassified stars was estimated using the morphological-independent redshift survey catalog from the Virmos VLT Deep Survey (VVDS, Le Fèvre et al. 2005), in particular the the $i < 22.5$ 22hr field. We selected the objects above 95% confidence level, which resulted in a catalog containing 5158 stars and 4264 galaxies. This catalog served as a truth table, to match galaxies in the coadd at $RA \sim -25°$. 908 spectroscopic stars and 3438 spectroscopic galaxies matched galaxies in the coadd catalog, indicating a contamination level of 18%. This is ~ 3 times higher than expected, assuming that the performance of the SDSS Star/Galaxy separator would be as good for the coadd as for the single pass data. The field in question is among the lowest galactic latitudes and highest stellar densities in the coadd, so this contamination rate is approximately an upper limit. The actual contamination rate would be roughly proportional to RA in the coadd.

We verified that most of the problematic objects are in a localized region of the psf−model vs. magnitude space, specifically inside the triangular region

$$\begin{aligned} r_{\rm psf} - r_{\rm model} &< 0.1 \cdot r_{\rm psf} - 2.1 \\ r_{\rm psf} - r_{\rm model} &> 0.03 \\ 21 < r_{\rm psf} &< 22.5 \end{aligned} \tag{23}$$

This indicates that an improved star galaxy separator can be designed using morphology and presumably color cuts.

5.4. *Star & Galaxy Catalog Completeness*

We used the package 2DPHOT (La Barbera et al. 2008) to measure the completeness of the coadd star and galaxy catalogs. This is done by adding simulated objects to the images and computing the recovery rate for both stars

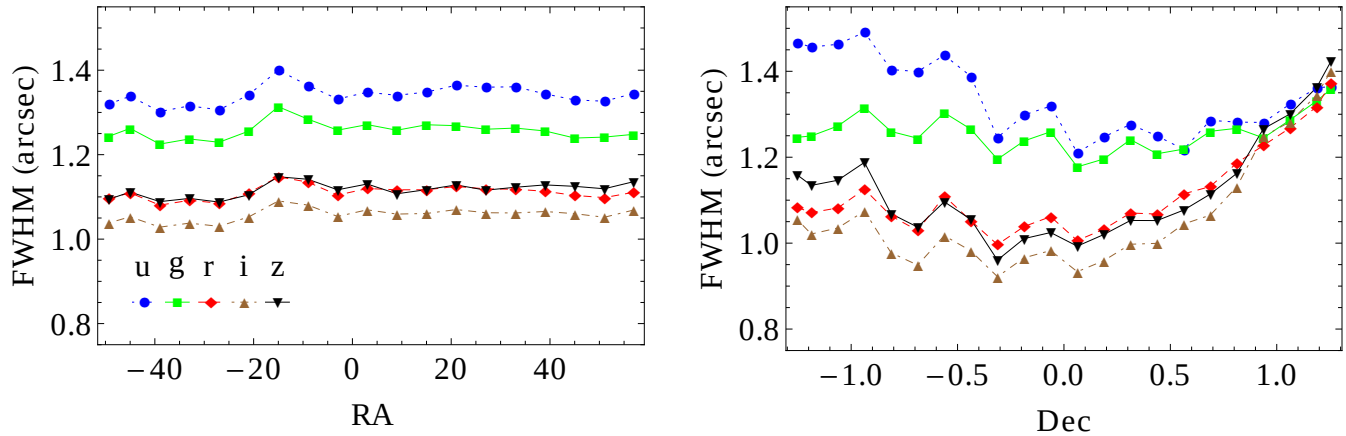

FIG. 4.— Left: Mean FWHM as a function of RA for the five filters. The range of seeing values is consistent with the expected Kolomgorov $\lambda^{-0.2}$ scaling with the exception of r and i bands. As the input images were selected in r and data in the other bands are taken at a few minutes removed in time in the order $riugz$, one might expect this behavior. Right: Mean FWHM as a function of Dec. At Dec > 0.5 the seeing gets worse as the camera optics begins to dominate (see, e.g., Stoughton et al. (2002)).

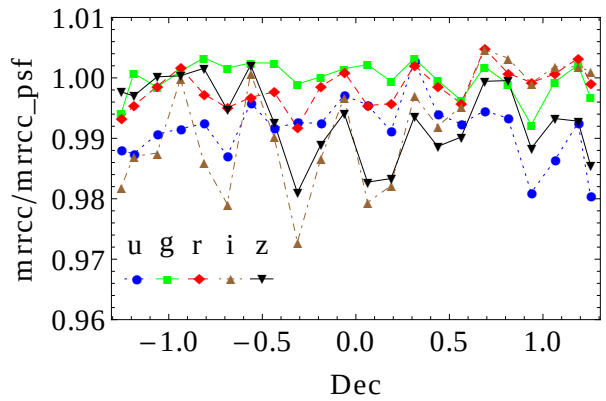

FIG. 5.— The declination projection of the ratio of size, measured through $m_r r_{cc}$, of stars and the psf evaluated at the star positions (`mrrcc/mrrcc_psf`). The ratio is accurately unity without dependence on declination, implying that the PSF modeling is accurate.

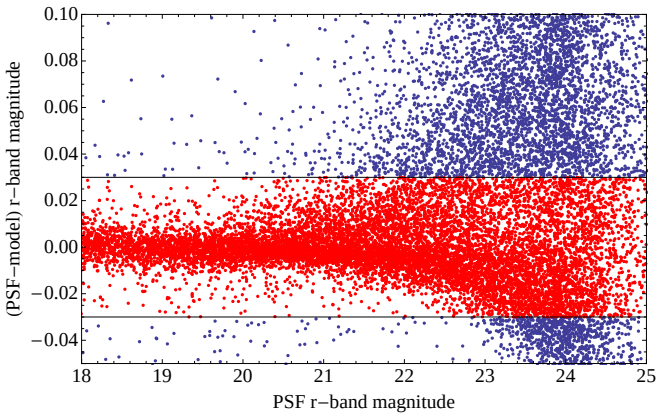

FIG. 6.— Star/galaxy separation based on PSF−model magnitude, $r_{\rm psf} - r_{\rm model}$. A model magnitude is the best galaxy deVaucouleurs or exponential profile convolved with the PSF in the sense of describing the data. In the event of a mismatch of the modeled PSF with the real PSF, or extended light, the model magnitude will measure more light than the PSF. It is thus a sensitive indicator of whether an object is well fit by the modeled PSF. Objects classified as stars are marked in red, galaxies in blue. There is a clear stellar locus at $r_{\rm psf} - r_{\rm model} \approx 0$. That the stellar locus bends towards negative values at $r_{\rm psf} > 22$ is likely due to errors in the PSF fit.

and galaxies. The parameters used to generate the objects are taken from the image itself. 2DPHOT first detects the objects in the image, performs star-galaxy separation and measures the photometric and structural (Sersic) parameters (`PHOTO` is not used in this process). Then it creates a list of objects that reproduces the magnitude and size distributions of the stars and galaxies found in the image and adds these simulated objects to the image. Finally, it measures the new image and computes the completeness as the fraction of objects recovered in each magnitude bin.

The resulting 2DPHOT completeness vs. magnitude curves, $C(m)$, are well fit by a Fermi-Dirac distribution function

$$C(m) = \frac{f_0}{1 + exp((m-\mu)/\sigma)} \tag{24}$$

where μ is the magnitude limit of the catalog (defined to be the magnitude at which $C(m) = 50\%$), f_0 is a normalization constant and the parameter σ controls how fast the completeness falls when it reaches the completeness threshold. We use this fitting function to determine the depth of the coadd galaxy and star catalogs, μ_G and μ_S respectively.

Our results are illustrated in Fig. 7. The plots on the first row show the r-band completeness for the same two fields pictured in Fig. 2. On the right we have the coadd field (run 206, camcol 3, field 505) and for comparison, on the left, one of the 28 single pass images used as input for that particular field. The coadd reaches $r = 24.3$ for point sources and $r = 23.4$ for galaxies, going about 2 magnitudes deeper than a single pass image, as expected. The plots on the second and third rows show the coadd results for the other filters. Table 5 is a compilation of the median and rms values of the coadd magnitude limits, calculated for 50 fields randomly selected.

5.5. *Color-Color Diagrams*

Stars populate a well-defined locus in the color-color space almost independent of magnitude. Therefore color-color diagrams are useful to access the quality of the photometry. Figure 8 shows the color-color diagrams of a isolated and well measured sample of coadd stars selected at $-5^\circ \leq$ RA $\leq 0^\circ$, in a high galactic latitude in Stripe 82 (see query in the Appendix). The sample

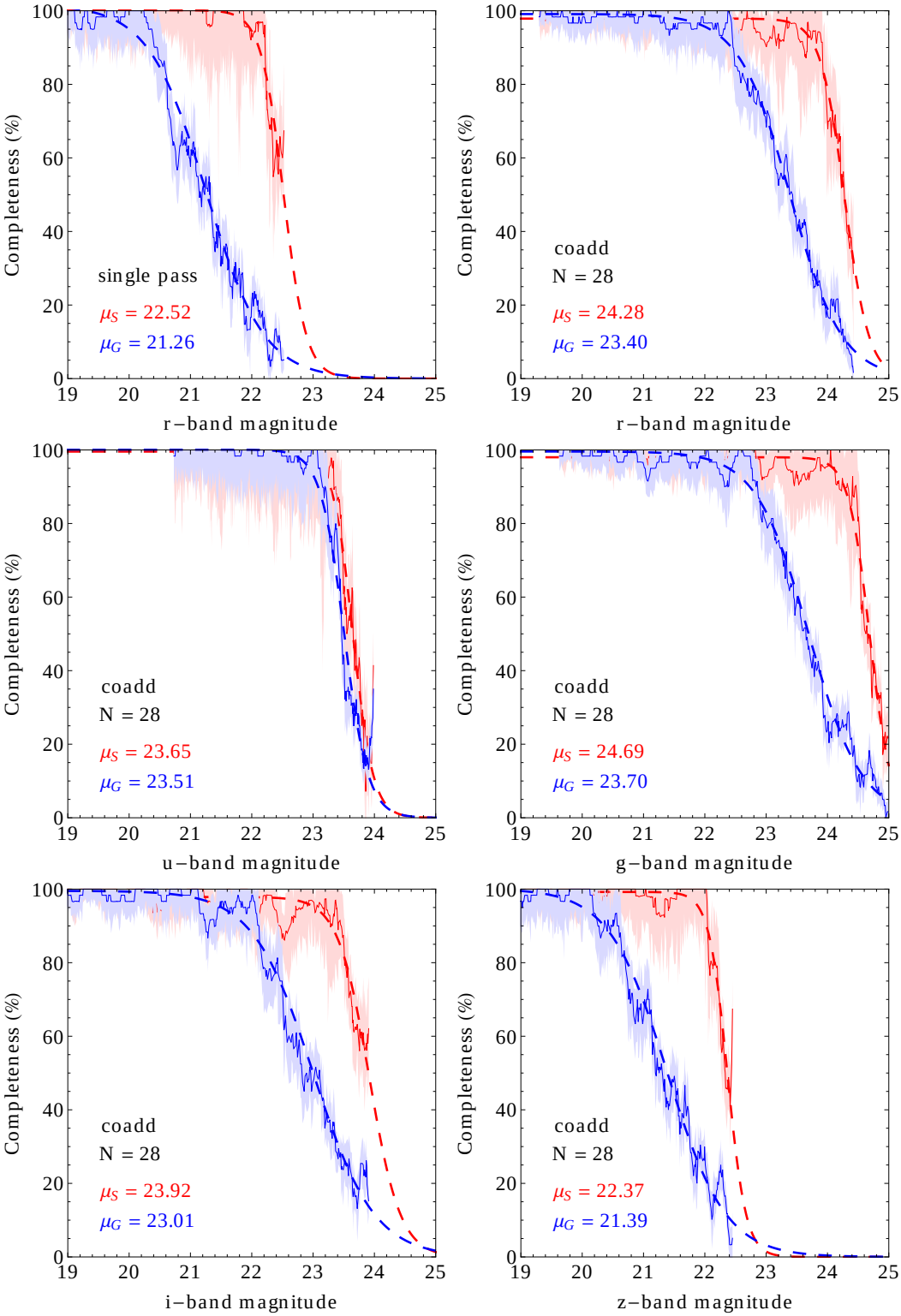

FIG. 7.— Completeness as function of r-band model magnitude for the coadd run 206, camcol 3, field 505 (corresponding to the image shown in Fig. 2). Point sources are represented in red, galaxies in blue. The solid lines are our measurements and the rms uncertainties are represented as light-colored regions. Dashed lines are the best fit model. There is a ≈ 0.09 mag scatter in the measurement of the completeness level as measured from frame to frame. The numbers refer to the 50% completeness level which we find to be a much more stable fit than the 95% level. Top: Comparison between the coadd (right) and one of the single pass images used in the coaddition (left), showing that we achieve ~ 2 mag deeper as $N = 28$ images contributed into this particular frame. Middle and bottom: Results for *griz* on the same frame, showing the typical depth of the coadd in each bandpass.

TABLE 5
50% Completeness Limits in the Coadd

filter	μ_S	$\sigma(\mu_S)$	μ_G	$\sigma(\mu_G)$
u	23.63	0.06	23.25	0.23
g	24.56	0.10	23.51	0.18
r	24.23	0.08	23.26	0.14
i	23.74	0.15	22.69	0.17
z	22.29	0.09	21.27	0.23

Note. — Coadd magnitude limits for stars (μ_S) and galaxies (μ_G). Values reported are medians and rms calculated for 50 fields randomly selected accross Stripe 82.

was split into 1 magnitude bins in r-band. At brighter magnitudes the intrisic thinness of the stellar locus is apparent. At fainter magnitudes statistical noise begins to dominate. Since this is an r-band sample, the u-band stars in the $20 < r < 21$ panel are quite faint; one cannot read from these diagrams where the signal to noise of the data degrades. One can read in these diagrams just how good the photometry can be for clean samples of stars.

For a reasons which we have not unearthed, the satureted flag did not propogate through `PHOTO`. Beware of objects with $m < 15.5$.

5.6. *Number Counts*

The number counts of stars and galaxies allow us to asses the depth of the coadd and the success of the star/galaxy separation. Figure 9 shows the i-band star and galaxy counts in regions of 5 deg^2 patches at a variety of galactic longitudes and latitudes along Stripe 82. The galaxy number counts show the Euclidean $m^{0.6}$ power law expected at $i < 20$, the slow change of slope due to cosmological volume and galaxy evolution at fainter magnitudes, and a roll off at $i \approx 23.5$ due to completeness issues. We have seen in panel 5 of Fig. 7 that the galaxy catalog is $\approx 50\%$ complete at $i = 23$, consistent with the deviation from the slowly rolling power law index seen here. We conclude that this plot shows nothing seriously wrong with the galaxy counts from $16 \leq i \leq 23.5$.

The star counts are going to be slightly more problematic. They are rough power laws that cross the galaxy counts at $i \approx 20$. The expected roll-over from incompleteness is apparent near $i \approx 23.5$. The steep rise in counts of stars seen easiest in the RA $= +57°$ patch data points is from galaxies being misclassified as stars: the galaxies outnumber the stars by $\gtrsim 30$ so even a small misclassification rate result in a large number of galaxies scattered into the star class, and one can see in Fig. 6 that at faint magnitudes the galaxy locus crosses the stellar locus. Once it does, stars can no longer be distinguished by galaxies using psf-model alone.

The models are from Trilegal star count modelling (Girardi et al. 2005, online version v1.4). In Figure 9 the galactic model parameters are those found by Jurić et al. (2008) using their SDSS star count tomographic mapping technique. The slope of the rough power-law is due to a combination of thin disk at brighter magnitudes and halo stars at fainter magnitudes. This model doesn't fit the data particularly well at the RA $= -31°$ patch, or at lower RA. Models with a lower exponential scale height, such as those derived from SDSS data using Trilegal model fits by B. Santiago (private communication) or from the SDSS m-dwarf fits of Bochanski et al. (2007) do describe the Stripe 82 data at RA $\lesssim -31°$. Figure 10 shows number counts in all five filters for the RA $= -31°$ field along with bands showing the range of star counts from the Santiago and Bochanski galactic models. This figure also shows, in all filters, the spike in counts as galaxies enter the star catalog in large numbers at faint magnitudes, and often a flattening of star counts at mag ~ 22. As we have seen in section §5.3 stars are entering the galaxy catalog in higher than expected numbers at these magnitudes due, most likely, to a PSF modelling problem, and the flattening is probably a reflection of this. Nevertheless, the data seems to indicate that there is an interesting problem in combining the deep Stripe 82 star counts with the single pass SDSS star counts. Overall, this and the previous figure show reasonable agreements between the Stripe 82 star counts and reasonable star count models.

6. SCIENCE

The coadd galaxy catalog is the largest homogeneous photometric catalog of its depth. It has 13 million galaxies and we have shown that it is complete to $r = 23.5$, being 2 magnitudes deeper than the SDSS single scan imaging survey. This implies that, despite covering an area 40 times smaller, the coadd volume has roughly 1/3 of the total volume of the SDSS data on the Northern Galactic Cap. The scientific questions that can be addressed by exploring this wealth of data are numerous and diverse. In this section we present a brief overview of recent and ongoing analyses using the coadd data.

The presence of deep imaging provides a template for variable object measurements and a means to check on the fainter objects of the single scan SDSS data. The SDSS-II Supernova Survey (Frieman et al. 2008) used the coadd images as a high-quality, photometrically calibrated template for carrying out image subtraction to discover supernovae. Later observations of the host galaxy often start with the coadd images (Lampeitl et al. 2010; Gupta et al. 2011) to locate the host. As much of the Stripe 82 data was taken as part of the SDSS-II SN survey, this use is expected.

There are many uses that are less tightly related to the goals of taking the data. For example, Liu et al. (2011) use the greater depth of the coadd as a means to check their science at the main survey limits, as they search for paired quasars in the SDSS and use the coadd to check for the fraction of interacting pairs missed due to the surface brightness limit of the single scan. Jiang et al. (2008) used the coadd to perform the the discovery of 5 quasars at redshift ~ 6 and to compute the high redshift quasar luminosity function. Vidrih et al. (2007) find white dwarf candidates. Our exploration of the Trilegal models in section §5.6 shows that these data could be used to constrain Galactic models.

Our main interest is in cosmology, and here there is a clear path of work. Photometric redshift measurements for the coadd galaxies were obtained by our group (Reis et al. 2011) using a neural network trained on spectroscopic redshifts obtained on Stripe 82. As Stripe 82 is easily accesible by telescopes in both the North and South hemispheres, the area has been well studied

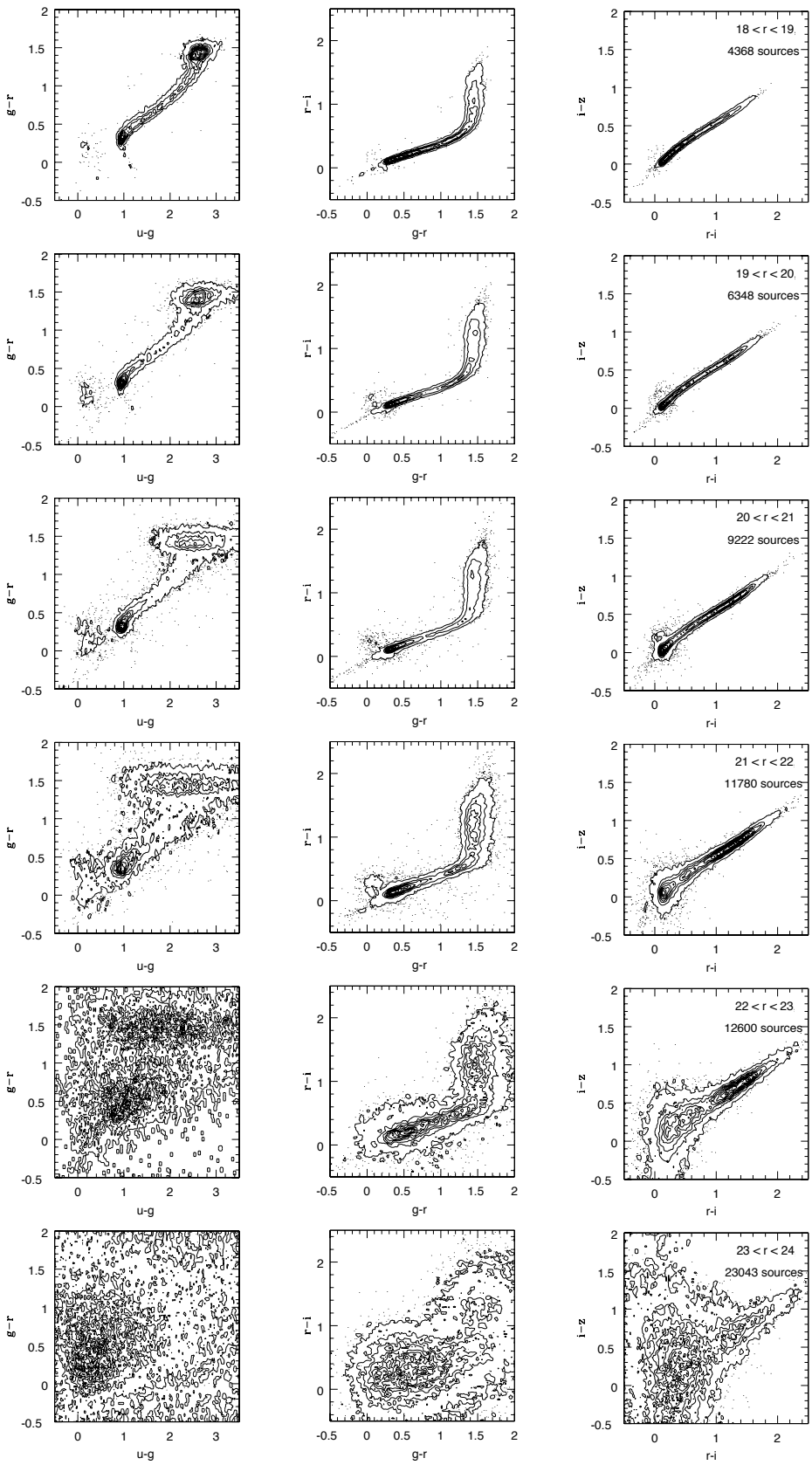

FIG. 8.— Color-color diagrams of stars in a 12 degree^2 field, in bins of 1 magnitude from $18 \leq r \leq 24$. Photon noise begins to dominate the bluer color in the $u-g$ vs $g-r$ plot at $r \geq 20$, the $g-r$ vs $r-i$ plot at $r \geq 21$, and the z band in the $i-z$ vs $r-i$ plot at $r > 21$. As the stellar locus is intriniscly very thin, these plots provide a sense of how good the photometry is at brighter magnitudes, and where statistical noise begins to dominate.

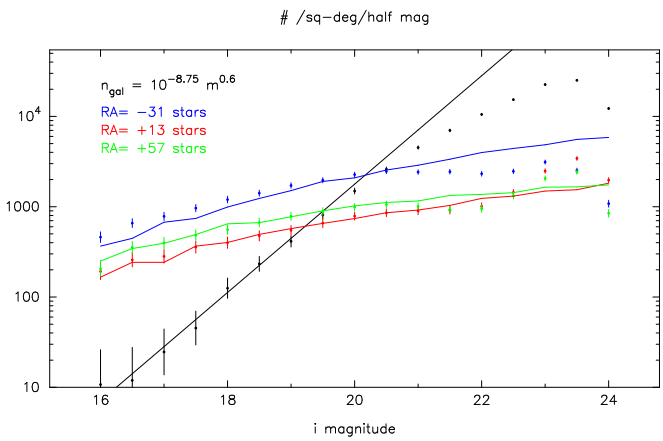

FIG. 9.— Star and galaxy counts in 5deg^2 patches: the data are points with poisson errors, and models are shown by lines. The three patches are at RA = −31°, Dec = 0° (l = 58°, b = −40°), RA = 13°, Dec = 0° (l = 123°, b = −63°), and RA = 57°, Dec = 0° (l = 188°, b = −40°). The galaxy counts (in black) show the expected Euclidean power law at $i < 20$, the slow change of slope due to cosmological volume and galaxy evolution at $20 < i < 23.5$, and the roll off at $i \approx 23.5$ due to completeness issues. The star count models fit the data well enough for the desired purpose, until $i \approx 23.5$, where there is a sudden upturn in star counts, most evident in the RA = 57° data. This is certainly due to galaxies being classified as stars.

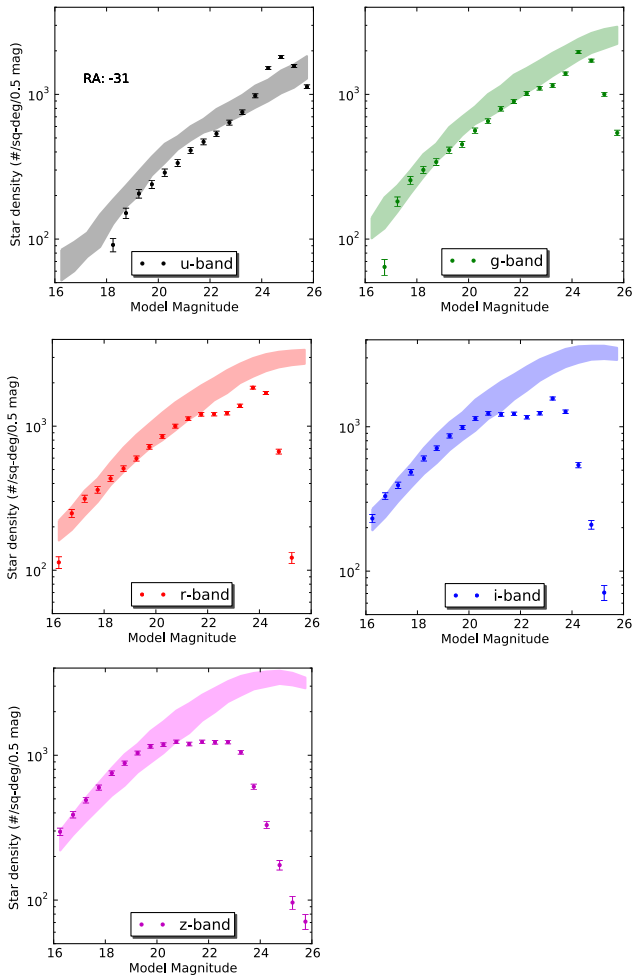

FIG. 10.— The Trilegal model star counts in u,g,r,i,z and coadd star counts at RA = −31°, Dec = 0° (b = −40°, l = 58°). The bands show a reasonable range of models, from one derived from Bochanski, the other from a private communication model of Santiago, modified to have the thin disk scale height z_o = 80 kpc.

spectroscopically. For the Reis et al. (2011) work, we used the Canadian Network for Observational Cosmology Field Galaxy Survey (CNOC; Yee et al. 2000), the Deep Extragalactic Evolutionary Probe (DEEP2; Weiner et al. 2005), the WiggleZ Dark Energy Survey (Drinkwater et al. 2010), the VIsible imaging Multi-Object Spectrograph Very Large Telescope Deep Survey (VVDS; Le Fèvre et al. 2005), and the SDSS-III Baryon Oscillation Spectroscopic Survey (BOSS; Eisenstein et al. 2011). The mean photo-z error acheived was $\sigma(z) = 0.034$ and the photo-z catalog is reliable out to $z \sim 0.8$, after which the low S/N of objects in the SDSS z-band becomes the limiting factor (see; Reis et al. 2011, for a detailed discussion). This photo-z catalog has been made public at the same time as this paper as a value-added catalog.

Since the photometric redshifts go to $z \approx 0.75$, an interesting program is cluster finding in the range $0.5 < z < 0.75$. Preliminary cluster catalogs have been pursued by our group using the Gaussian Mixture Brightest Cluster Galaxy (GMBCG; Hao et al. 2010) and the Voronoi Tessellation cluster finder in 2+1 dimensions (Soares-Santos et al. 2011, VTT) algorithms. We plan on pursing a search for blue clusters using the VTT as a finder and the GMMBCG as a red sequence measuring engine aiming at studying cluster formation and evolution.

In Lin et al. (2011) we report the measurement of cosmological parameters from the cosmic shear signal in the coadd. All weak lensing analyses require accurate shape estimation parameters, but the cosmic shear is an extreme case, due to its very low signal. `PHOTO` measures second moments and related parameters needed for weak lensing, but several systematic errors in the PSF had to be corrected. Some of these systematic were doubt due to our mis-modelling of the PSF because of the mis-matched weights (see section §5.2). After the corrections and weak lensing-specific quality cuts, the coadd data provides ∼ 6 galaxies per arcmin^2 for the analysis, 6 times more than the SDSS single pass data. Huff et al. (2011), in an independent work, have also measured the cosmic shear on Stripe 82. They did not use the coadd described in this paper, but instead, made their own coadd optimizing for weak lensing.

A related program is to measure the masses of clusters found in the SDSS Coadd area. The MaxBCG (Koester et al. 2007) cluster catalog overlaps with Stripe 82 using single pass data (as do other cluster catalogs, e.g., Geach et al. (2011); Dong (2011); Szabo et al. (2011)).

We have performed a stacked cluster weak lensing analysis with the MaxBCG clusters as lenses and the coadd galaxies as sources (Simet et al. 2011). We divide our cluster sample in bins of richness and measure a mass-richness relation consistent with previous work (Johnston et al. 2007). This demonstrates that the coaddititon process does not dilute the lensing signal. As we detect an increasing signal as a function of source redshift we also conclude in Simet et al. (2011) that we have detected weak lensing tomography signal in the coadd.

Since the survey covers a large area on a part of the sky that has been heavily studied there are also many

opportunities for multi-wavelength studies, from the x-ray (XMM: Mehrtens et al. 2011) to the microwave (SZ: Menanteau et al. 2010; Hand et al. 2011; Reese et al. 2011; Sehgal et al. 2011).

It is unlikely that we have surveyed all of the science the coadd has been put to use for, as it is part of the DR7 database and easily accesible by the community. This paper serves as as a technical description of this widely available dataset.

7. CONCLUSIONS

The SDSS performed repeat scanning of the equatorial region in the South Galactic Cap known as Stripe 82. The amount of data observed was comparable to the single scan coverage of the SDSS footprint. The aim of the work described here was to coadd this data and analyze it using the SDSS pipeline framework, notably the `PHOTO` pipeline. Roughly a third of the existing Stripe 82 data was coadded, limited in time by when the work was performed. The runs included calibrated and uncalibrated data, so a relative calibration scheme was developed and applied. The images were mapped onto a SDSS run format output grid using the SDSS astrometry, were coadded using a S/N weighting that includes seeing, and inverse variance maps computed. The coadded images were run through `PHOTO` using PSF models computed by coadding the PSFs.

The resulting catalogs have median seeing in r of $1.1''$ and varies band to band following Kolmogorov scalings. The catalogs are 50% complete to $r = 23.5$ (galaxies) and $r = 24.3$ (stars). The photometry is good to 0.5% in g,r,i, and 1% in u and z, as measured against the Ivezić et al. (2007) star catalog. The PSF is modeled and despite minor issues it is useful for precision photometry. Color-color diagrams of stars show a sharp and thin stellar locus, and the number counts of stars at a variety of positions show agreement with reasonable galactic models. There are identifiable regions in psf-model vs magnitude space where stars are being misclassified as galaxies, and we give suggestions on how to eliminate these. Thus we have constructed high quality SDSS catalogs on the Stripe 82 region from images that are two magnitudes deeper than the single pass SDSS data.

The coadd catalog is largest homogeneous precision photometric catalog complete to r=23.5. The catalog has 13 million galaxies, and has a variety of uses from galactic structure to large scale structure and weak lensing, to cosmology. The data, including both images and catalogs, are available through the standard SDSS distribution channels.

This research was done using resources provided by the Open Science Grid, which is supported by the National Science Foundation and the U.S. Department of Energy Office of Science.

Funding for the SDSS and SDSS-II has been provided by the Alfred P. Sloan Foundation, the Participating Institutions, the National Science Foundation, the U.S. Department of Energy, the National Aeronautics and Space Administration, the Japanese Monbukagakusho, the Max Planck Society, and the Higher Education Funding Council for England. The SDSS Web Site is http://www.sdss.org/.

The SDSS is managed by the Astrophysical Research Consortium for the Participating Institutions. The Participating Institutions are the American Museum of Natural History, Astrophysical Institute Potsdam, University of Basel, University of Cambridge, Case Western Reserve University, University of Chicago, Drexel University, Fermilab, the Institute for Advanced Study, the Japan Participation Group, Johns Hopkins University, the Joint Institute for Nuclear Astrophysics, the Kavli Institute for Particle Astrophysics and Cosmology, the Korean Scientist Group, the Chinese Academy of Sciences (LAMOST), Los Alamos National Laboratory, the Max-Planck-Institute for Astronomy (MPIA), the Max-Planck-Institute for Astrophysics (MPA), New Mexico State University, Ohio State University, University of Pittsburgh, University of Portsmouth, Princeton University, the United States Naval Observatory, and the University of Washington.

APPENDIX

QUERY FOR CLEAN PHOTOMETRY STARS

Here we provide the query used to obtain the sample of isolated and well measured stars used for the color-color diagrams. The query is to be run on the `Stripe 82` database of the SDSS Catalog Arquive Server (CAS).

```
SELECT u,g,r,i,z,
psfMag_u,psfMag_g,psfMag_r,psfMag_i,psfMag_z,flags,
ra,dec, run, camcol, field,
psfmagerr_u, psfmagerr_g, psfmagerr_r, psfmagerr_i, psfmagerr_z
FROM PhotoObjAll
WHERE ((flags  0x10000000) != 0)
AND ((flags  0x8100000c00a4) = 0)
AND (((flags  0x400000000000) = 0) or
(psfmagerr_r <= 0.2 and psfmagerr_i<= 0.2 and psfmagerr_g<=0.2))
AND (((flags  0x100000000000) = 0) or (flags  0x1000) = 0)
AND (run = 106 or run = 206)
AND type = 6
AND mode = 1
AND ra between 355 and 0
```

REFERENCES

Abazajian, K. et al. 2004, AJ, 128, 502

—. 2003, AJ, 126, 2081

Abazajian, K. N. et al. 2009, ApJS, 182, 543
Aihara, H. et al. 2011, ApJS, 193, 29
Bertin, E., Mellier, Y., Radovich, M., Missonnier, G., Didelon, P., & Morin, B. 2002, in Astronomical Society of the Pacific Conference Series, Vol. 281, Astronomical Data Analysis Software and Systems XI, ed. D. A. Bohlender, D. Durand, & T. H. Handley, 228–+
Blanton, M. R., Kazin, E., Muna, D., Weaver, B. A., & Price-Whelan, A. 2011, ArXiv e-prints
Bochanski, J. J., Munn, J. A., Hawley, S. L., West, A. A., Covey, K. R., & Schneider, D. P. 2007, AJ, 134, 2418
Bramich, D. M. et al. 2008, MNRAS, 386, 887
Dong, F. 2011, PhD thesis, Princeton University
Drinkwater, M. J. et al. 2010, MNRAS, 401, 1429
Eisenstein, D. J. et al. 2011, AJ, 142, 72
Frieman, J. A. et al. 2008, AJ, 135, 338
Fukugita, M., Ichikawa, T., Gunn, J. E., Doi, M., Shimasaku, K., & Schneider, D. P. 1996, AJ, 111, 1748
Geach, J. E., Murphy, D. N. A., & Bower, R. G. 2011, MNRAS, 413, 3059
Girardi, L., Groenewegen, M. A. T., Hatziminaoglou, E., & da Costa, L. 2005, A&A, 436, 895
Gunn, J. E. et al. 1998, AJ, 116, 3040
—. 2006, AJ, 131, 2332
Gupta, R. R. et al. 2011, ApJ, 740, 92
Hand, N. et al. 2011, ApJ, 736, 39
Hao, J. et al. 2010, ApJS, 191, 254
Hogg, D. W., Finkbeiner, D. P., Schlegel, D. J., & Gunn, J. E. 2001, AJ, 122, 2129
Huff et al. 2011, preprint
Ivezić, Ž. et al. 2004, Astronomische Nachrichten, 325, 583
—. 2007, AJ, 134, 973
Jiang, L. et al. 2008, AJ, 135, 1057
Johnston, D. E. et al. 2007, ArXiv e-prints
Jurić, M. et al. 2008, ApJ, 673, 864
Koester, B. P. et al. 2007, ApJ, 660, 239
La Barbera, F., de Carvalho, R. R., Kohl-Moreira, J. L., Gal, R. R., Soares-Santos, M., Capaccioli, M., Santos, R., & Sant'anna, N. 2008, PASP, 120, 681
Lampeitl, H. et al. 2010, ApJ, 722, 566
Le Fèvre, O. et al. 2005, A&A, 439, 877
Lin et al. 2011, preprint
Liu, X., Shen, Y., Strauss, M. A., & Hao, L. 2011, ApJ, 737, 101
Lupton, R., Gunn, J. E., Ivezić, Z., Knapp, G. R., & Kent, S. 2001, in Astronomical Society of the Pacific Conference Series, Vol. 238, Astronomical Data Analysis Software and Systems X, ed. F. R. Harnden Jr., F. A. Primini, & H. E. Payne, 269–+
Lupton, R. H., Gunn, J. E., & Szalay, A. S. 1999, AJ, 118, 1406
Lupton, R. H., Ivezić, Ž., Gunn, J. E., Knapp, G. R., & Strauss, M. A. 2012, The photo-lite draft, plus other notes at RHL's website http://www.astro.Princeton.EDU/ rhl/photo-lite.pdf
Mehrtens, N. et al. 2011, ArXiv e-prints
Menanteau, F. et al. 2010, ApJ, 723, 1523
Oke, J. B., & Gunn, J. E. 1983, ApJ, 266, 713
Padmanabhan, N. et al. 2008, ApJ, 674, 1217
Pier, J. R., Munn, J. A., Hindsley, R. B., Hennessy, G. S., Kent, S. M., Lupton, R. H., & Ivezić, Ž. 2003, AJ, 125, 1559
Reese, E. D. et al. 2011, ArXiv e-prints
Reis et al. 2011, preprint
Richards, G. T. et al. 2002, AJ, 123, 2945
Schlegel, D. J., Finkbeiner, D. P., & Davis, M. 1998, ApJ, 500, 525
Sehgal, N. et al. 2011, ApJ, 732, 44
Simet et al. 2011, preprint
Smith, J. A. et al. 2002, AJ, 123, 2121
Soares-Santos, M. et al. 2011, ApJ, 727, 45
Stoughton, C. et al. 2002, AJ, 123, 485
Szabo, T., Pierpaoli, E., Dong, F., Pipino, A., & Gunn, J. 2011, ApJ, 736, 21
Tucker, D. L. et al. 2006, Astronomische Nachrichten, 327, 821
Vidrih, S., Bramich, D. M., Hewett, P. C., Evans, N. W., McMahon, R. G., et al. 2007, MNRAS, 382, 515
Weiner, B. J., et al. 2005, ApJ, 620, 595
Yee, H. K. C. et al. 2000, ApJS, 129, 475
York, D. G. et al. 2000, AJ, 120, 1579
Zacharias, N. et al. 2000, AJ, 120, 2131